Check for updates

Strengthening of Mg–Al–Ca alloys with C15 and C36 Laves phases

Muhammad Zubair[1,2,a)] , Stefanie Sandlöbes-Haut[1], Risheng Pei[1],
Maximilian A. Wollenweber[1], Lukas Berners[1], Carl F. Kusche[1], Chuanlai Liu[3], Franz Roters[3],
James S. K.-L. Gibson[1], Sandra Korte-Kerzel[1,a)]

[1] Institute for Physical Metallurgy and Materials Physics, RWTH Aachen University, Kopernikusstr. 14, 52074 Aachen, Germany
[2] Present Address: Department of Metallurgical & Materials Engineering, Faculty of Chemical, Metallurgical & Polymer Engineering, University of Engineering & Technology (UET) Lahore, Lahore, Pakistan
[3] Max-Planck-Institut Für Eisenforschung, Max-Planck-Str. 1, 40237 Düsseldorf, Germany
a) Address all correspondence to these authors. e-mails: zubair@uet.edu.pk; korte-kerzel@imm.rwth-aachen.de

Laves phases such as $CaMg_2$ (C14), $Ca(Al,Mg)_2$ (C36), and $CaAl_2$ (C15) have high melting points, high hardness at room and elevated temperatures, but are inherently brittle. Cast Mg–Al–Ca alloys having Laves phase skeleton thus have good creep properties but limited ductility. An understanding of the co-deformation behaviour of α-Mg and Laves phases is essential for further improving the mechanical performance of these alloys. Here, we study the mechanical behaviour of a Mg–4.65Al–2.82Ca alloy using micropillar compression in the α-Mg matrix, at α-Mg/C36 and α-Mg/C15 interfaces and in the C15 phase in combination with scanning electron microscopy. We show that both, C15 and C36 phases, provide considerable strengthening to the α-Mg matrix. The amount of strengthening primarily depends on the volume fraction and geometry of Laves phases in composite micropillars and correlates well with the iso-strain and iso-stress bounds predicted for α-Mg/C36 and α-Mg/C15 composites.

Introduction

Laves phase containing Mg–Al–Ca alloys exhibit superior creep resistance when compared to conventional Mg–Al–Mn or Mg–Al–Zn alloys [1–3]. These Laves phases reinforcing the Mg–Al–Ca alloys are characterised by high strength [4], hardness [4–7] and melting points [5] when compared to the α-Mg matrix [6]. In cast Mg–Al–Ca alloys, the Laves phases are present as an intra- and intergranular skeleton within the α-Mg matrix [6, 8–11]. Knowledge about the amount of strengthening induced by Laves phases in the Mg matrix is important and can be helpful for alloy design. However, even where overall strengthening of an alloy is observed due to the introduction of a second phase, it is the understanding of which deformation mechanisms are affected, and in which way, that really opens purposeful microstructure and composition design strategies.

Previous work on Mg–Al–Ca alloys has mainly focussed on the identification of advantageous microstructures with respect to the formation of an intermetallic skeleton and the macroscopic properties that can be obtained as a result [2, 8, 11–13]. For those alloys with the most promising properties,

the co-deformation mechanisms were also explored [6, 10]. These alloys have in common that they contain the $Ca(Mg,Al)_2$ C36 phase as the dominant strengthening Laves phase. What is not known is whether one of the other Laves phases of the Mg–Al–Ca system may in principle give better co-deformation performance in offering equally or better high temperature stability, load-shielding to enhance creep resistance or co-deformation of the matrix and intermetallic skeleton at stress concentrations to avoid cracking and void formation that lead to early failure. In this respect, the cubic $CaAl_2$ phase is of particular interest. It is known to be harder than the other Laves phases [5, 14, 15], making it possibly harder to co-deform, but as a cubic phase also likely offers a larger number of slip systems, which may align with the basal plane of the hexagonal Mg matrix to allow dislocations to cross the interface.

The most easily activated deformation mechanisms of Mg at room temperature are basal slip and extension twinning. This is because the critical resolved shear stresses, τ_{CRSS}, required to activate basal slip and extension twinning, amount to ≈ 0.5 MPa [16, 17] and < 10 MPa [18, 19], respectively. On

the other hand, the stresses required to activate prismatic and pyramidal < a > slip in Mg are ≈ 39–44 MPa [20–23]. This large difference between the τ_{CRSS} for activation of different deformation mechanisms usually results in a strong plastic anisotropy at ambient temperature [24, 25]. Consequently, large differences are found between the yield stresses when the crystals are deformed along different directions [26–28]. Considering this, if micropillar testing is carried out on different crystal orientations in a comparison of micropillars from the two different microstructural regions (α-Mg and α-Mg/Laves phase interfaces), then the orientation dependence of deformation in the α-Mg matrix has to be taken into account as well for any specimens consisting of both phases, particularly as deformation is bound to start in the softer metallic phase.

Depending on the Ca/Al ratio and the temperature chosen for any annealing treatment, there can be three different types of Laves phases in Mg–Al–Ca alloys: $CaAl_2$ (C15), $CaMg_2$ (C14) or $Ca(Mg,Al)_2$ (C36) phase [8, 14, 29–32]. The cubic C15 phase is generally reported in as-cast Mg–Al–Ca alloys where the Ca/Al ratio is ≈ ≤ 0.3 [30, 33]. The C36 and C14 phases tend to be present in alloys where the Ca/Al ratio is below or above approximately 2/3, respectively [8, 30, 31, 34–38]. These ratios can change depending on the cooling rate during solidification and often two Laves phases tend to coexist, e.g. a combination of C36 and C14 phase was reported in Mg-5.37Al-2.89Ca (Ca/Al: 0.54) [30], in Mg-3.68Al-3.8Ca (Ca/Al: 1.03) [8] and in Mg–3.94Al–3.83Ca (Ca/Al: 0.97) [14]. Nonetheless, as the Ca/Al ratio varies from 0.3 to 1 and beyond, the nature of the present Laves phase changes from C15 to C36 and finally to C14 as the Ca/Al ratio increases [14, 30, 35, 39].

Although they are macroscopically brittle at low temperatures, Laves phases have shown considerable plasticity in small scale mechanical testing like micropillar compression [4, 7, 15, 40]. The thickness of Laves phase struts in conventional as-cast Mg–Al–Ca alloys is of the order of 1 μm or less; close to the dimensions generally studied in micropillar compression testing.

Here, our aim is to achieve insights into the co-deformation of the Mg matrix with two different Laves phases under conditions close to those in a final, technologically useful microstructure. Due to the morphology of the Laves phase available from as-cast microstructures, with their finer Laves precipitates, certain information will remain out of reach, e.g. an accurate interfacial shear strength or quantitative transmission stresses. However, even though the occurring phase transformations make the preparation of interfaces for dedicated mechanical testing a challenging endeavour, this information may be studied separately in the future if straight interfaces can be achieved by appropriate heat treatment or solidification conditions.

In this work, we therefore set out to study the active deformation mechanisms and in particular co-deformation in a Laves phase reinforced Mg–Al–Ca alloy. For this, we considered four systematic sets of conditions: (1) (micro)compression of the α-Mg phase in different orientations to assess the behaviour of the matrix alloyed with Al and Ca as a baseline, (2) compression of micropillars containing α-Mg/Laves phases interfaces with the C36 Laves phase from as-cast alloy or (3) Mg/C15 Laves phase interfaces from the same alloy in an annealed state and (4) compression of C15 Laves phase. Together, these allow us to directly compare the strengthening effect of the Laves phases on the α-Mg matrix and assess the effects of the geometrical alignment of Laves phases on the co-deformation behaviour.

Results

Microstructural characterisation

A typical secondary electron (SE) image of the as-cast microstructure of cast Mg–4.65Al–2.82Ca is presented in Fig. 1(a). The α-Mg matrix (grey colour) is reinforced with an interconnected intermetallic skeleton (white phase) shown at greater magnification in Fig. 1(b). The grain size of the alloy is large when compared to the areas bounded by the intermetallic struts [Fig. 1(c)]. The big grains enabled milling of micropillars from a single grain within the α-Mg matrix and at the α-Mg/Laves phase interfaces. The determined composition using energy dispersive spectroscopy (EDS) in scanning transmission electron microscopy (STEM) of the intermetallic Laves phase and the α-Mg matrix is presented in Fig. 1(d) (data taken from [14]). Note that the solubility of Ca in the α-Mg matrix is very low and therefore not quantified here by means of EDS. The morphology, composition, and structural analysis (as presented in [14]) of the Laves phase confirms that it is the $Ca(Mg,Al)_2$ C36 phase. The C36 phase was also determined to be the main intermetallic phase in similar alloys studied previously [9–11, 37]. This phase is also shown to contain small precipitates as highlighted by green arrows Fig. 1(e). These have been characterized as Mg rich precipitates within the C36 phase [41]. Moreover, there are intragranular needle-like $CaAl_2$ C15 precipitates within the α-Mg matrix in line with the previously reported work on similar alloys [8, 11].

The microstructure of the heat-treated alloy contains the α-Mg matrix and inter- and intragranular C15 Laves phase precipitates (Fig. 2). The C15 precipitates were present as irregular particles or thick platelets in comparison to thin interconnected struts in the as-cast alloy, [Fig. 2(a and b)]. Moreover, the present intermetallic phase changed after heat treatment: in the as-cast alloy, the C36 Laves phase was observed, while in the heat-treated sample the C15 phase was observed [Fig. 2(c)]. The heat treatment effects on microstructure evolution in this alloy have already been presented in [14], where the Mg and C36 phase were found to be stable
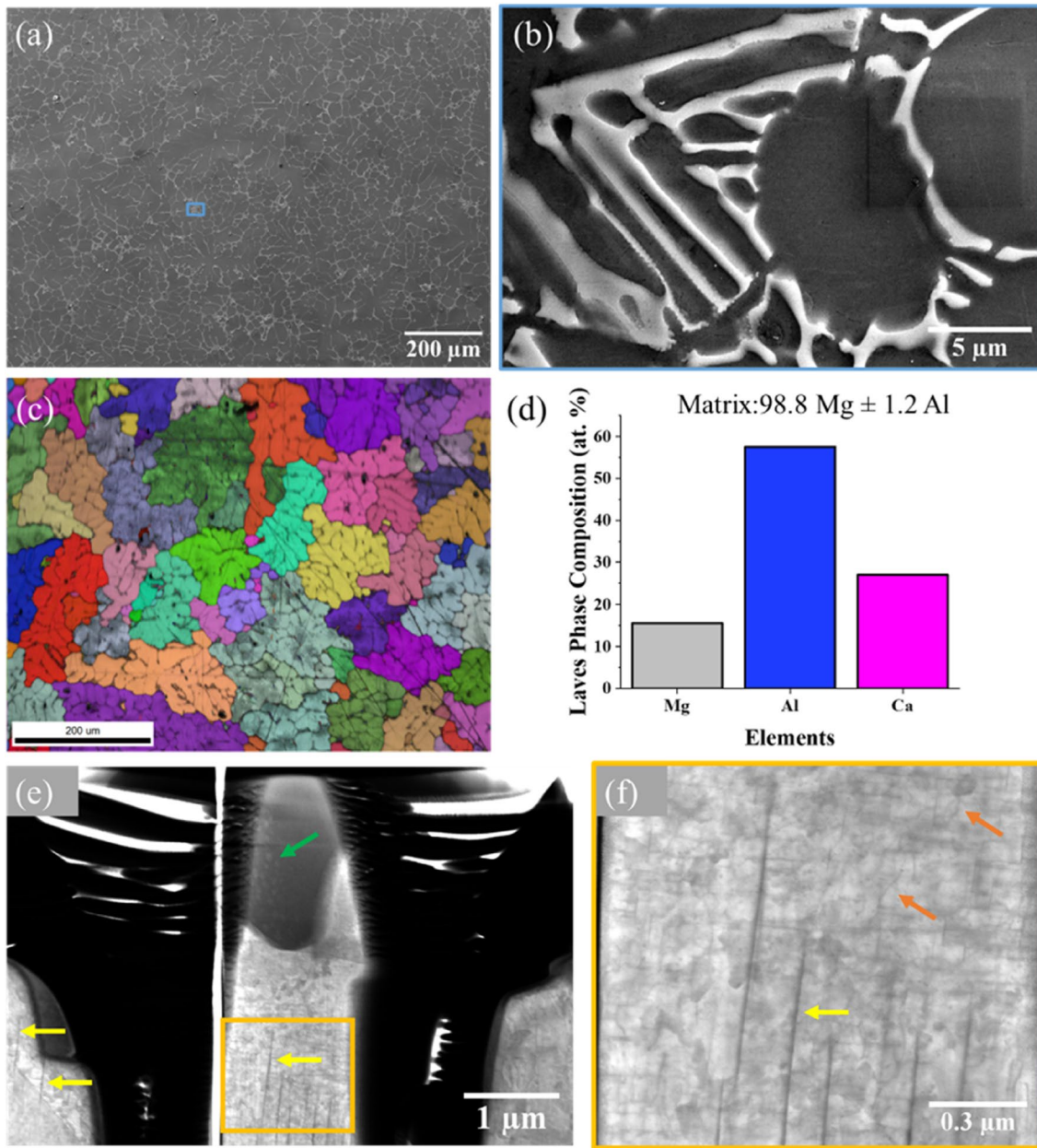
Figure 1: (a) SE image showing the microstructure of the as-cast Mg-4.65Al-2.82Ca alloy, (b) is the high magnification image of the microstructural region highlighted by blue rectangle in (a), (c) shows the inverse pole figure (IPF) and image quality (IQ) maps superimposed on each other showing that the grain size exceeds the distance between intermetallic struts (IPF legend is same for Mg phase as presented in Fig. 2) and (d) depicts the composition of the microstructural constituents determined using STEM-EDS (composition taken from [14]). (e) STEM image of a cross-section through a micropillar from the as-cast material containing C36 Laves phase as the darker phase with precipitates (green arrow) and α-Mg matrix with dislocations (orange arrows) and CaAl$_2$ precipitates (yellow arrows) including a magnified view of the orange rectangle.

at a temperature of 500 °C (heat treatment temperature) in Mg–4.65Al–2.82Ca alloy by CALPHAD modelling. However, the stability of the C36 phase in this alloy decreases with temperature and during cooling the C36 phase transforms to C15.

The area fraction of the Laves phase is reduced from ∼ 7.1% C36 in the as-cast state to ∼ 4.9% C15 phase in the heat-treated state [14]. This reduction in area fraction is assumed to occur because the C36 phase contains a larger amount of Mg than the C15 phase [42].
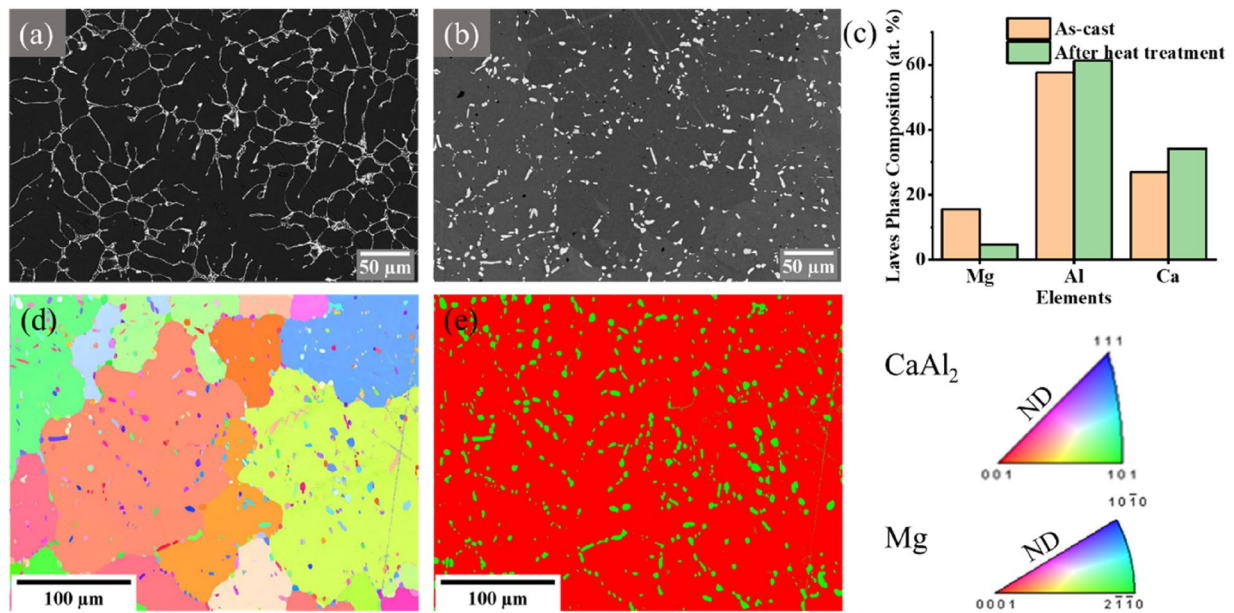
Figure 2: (a) Microstructure of the as-cast alloy, (b) microstructure of the heat-treated alloy, (c) change in composition of the intermetallic phase after heat treatment, (d) IPF map of Mg and $CaAl_2$ phase and (e) phase map of the same region shown in (d) having Mg (in red) and $CaAl_2$ in green. ND is the surface normal direction pointing towards the reader (for further details see Figure SM 1).
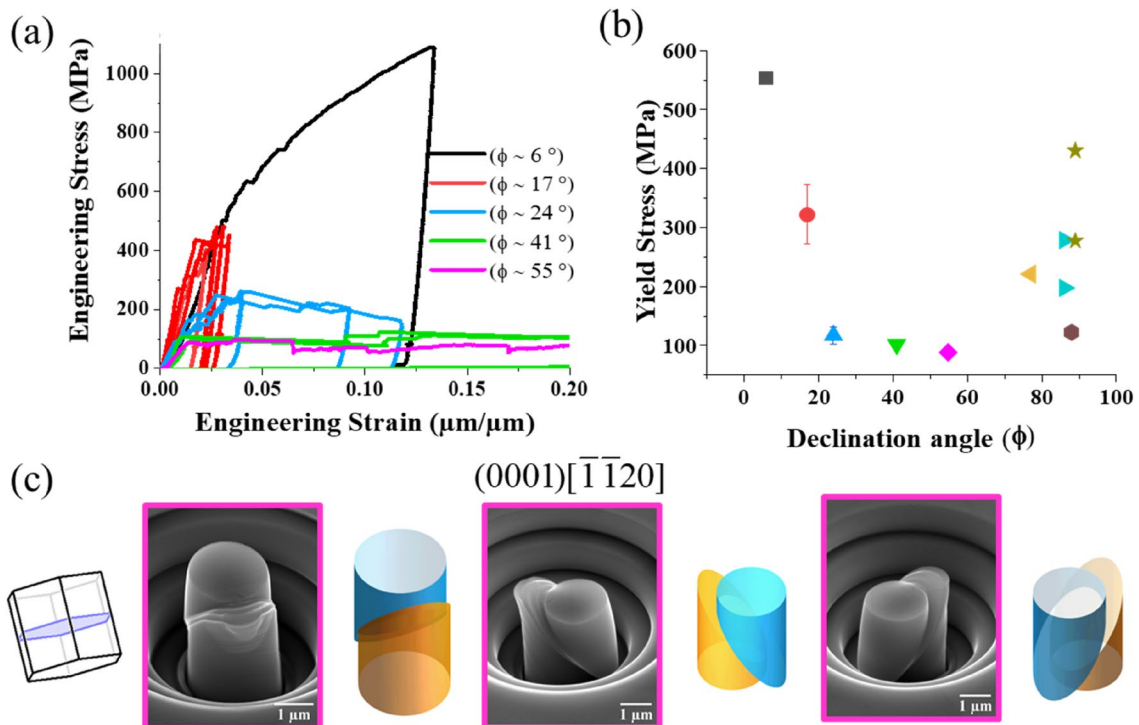
Figure 3: (a) Engineering stress–strain curves of Mg micropillars deformed at room temperature for low to intermediate declination angles ϕ, (b) variation of the yield stress ($\sigma_{0.2}$) with ϕ, (c) SE images of the side view taken at an angle of 45° to the surface normal of a deformed micropillar from three different directions and their comparison with simulated micropillars depicting the activation of basal slip.

Deformation of the α-Mg phase—effect of c-axis orientation

The micropillars were milled into α-Mg grains with declination angles (ϕ) between the compression axis and the c-axis of the Mg unit cell varying from ~ 6 to ~ 89°. As expected for Mg, the engineering stress–strain curves showed a strong dependence on the orientation [Fig. 3(a)]. The yield stress first decreased up to intermediate angles [see also Fig. 3(a)] and then increased again towards 89° [Fig. 3(b)]. Basal slip was found to be the predominant deformation mechanism at the angles tested with ϕ up to 55° [the next considered inclination was 77°, all tested angles are shown in Fig. 3(b)]. The slip system identification was confirmed by matching the deformed pillars with simulated pillars which were generated using the Matlab code and electron backscatter diffraction (EBSD) data as discussed in [43, 44]. For this purpose, the deformed and simulated pillars were compared from three different sides and rotated clockwise at increments of 120° [Fig. 3(c)]. The deformation features in micropillars undergoing basal slip were very similar to the earlier reported cylindrical Mg micropillars oriented for basal slip [45–47].

Extension twinning or a combination of extension twinning and basal slip (within the deformation twin) was observed when ϕ was varied between 77 and 89° (Fig. 4). In a few micropillars, only basal slip was also observed together with bending of the micropillars [one such example is shown in Fig. 4(e)]. A side and top view image of one deformed micropillar with the c-axis nearly perpendicular to the applied load is presented in [Fig. 4(a and b)]. As opposed to basal slip, it is not straight forward to

confirm extension twinning in the deformed micropillars. We therefore used post-deformation orientation analysis by transmission kikuchi diffraction (TKD) to confirm the occurrence of twinning by lifting out a thin lamella. The position from where the lamella was lifted out is highlighted by the white dotted rectangle in Fig. 4(b). The IPF map of the deformed cross-section [Fig. 4(c and d)] reveals that the entire micropillar has twinned and analysis of the misorientation angle between the undeformed matrix and the deformed pillar confirms that the twin is a $\{10\bar{1}2\}$ extension twin commonly observed in Mg.

Co-deformation of the α-Mg(Al,Ca) and hexagonal C36 Laves phase

In micropillars containing both phases in the as-cast alloy, i.e. Mg matrix and mainly C36 Laves phase, the Laves phase skeleton can delay the onset of basal slip and twinning, but the effectiveness of this strengthening effect depends on the geometric alignment of intermetallic phase and the active deformation paths originating from the Mg matrix (Fig. 5).

There is a significant increase in yield stress when the Laves phase runs through the micropillar [Fig. 5(a–c)]. The strengthening effect of the Laves phase was much weaker when the Laves phase was present only in a portion of the micropillar [Fig. 5(d–f)] and therefore parts of the pillars were able to deform on a continuous basal slip plane in the Mg phase alone. The small strengthening contribution was then presumably due to the slight radius increase along the pillar axis [Fig. 5(f)] as the strengthening induced by Laves phase in the upper portion
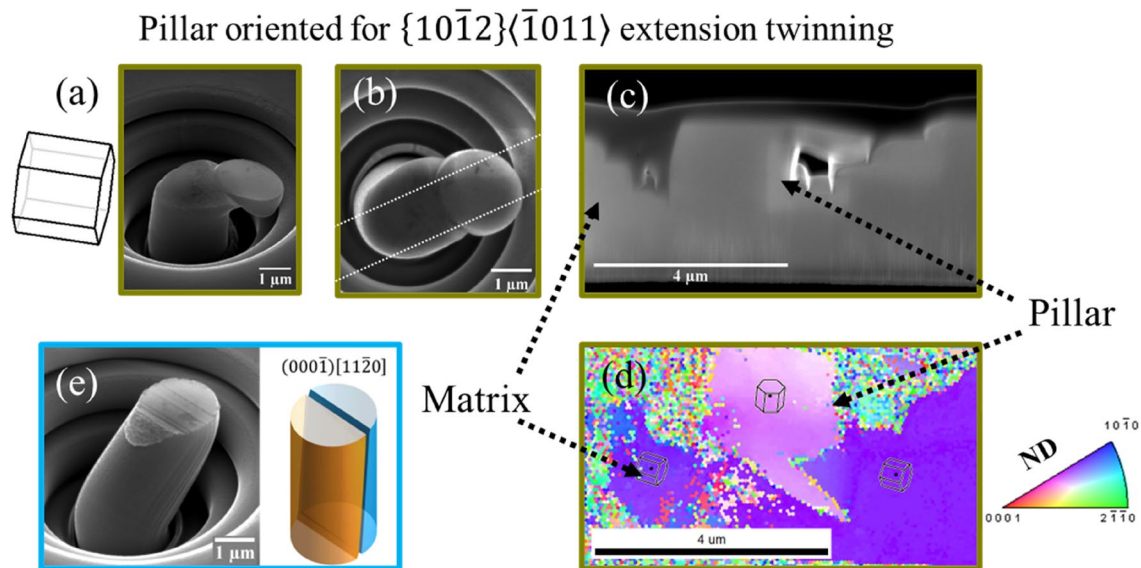
Figure 4: (a): side view (SE image) of a deformed micropillar oriented for extension twinning (unit cell and micropillar image is at 45° tilt), (b) top view of the micropillar shown in (d). The white dotted rectangle in (b) depicts the region from where the focussed ion beam (FIB) lamella was lifted out for TKD, (c) micropillar cross-section on which TKD was performed, (d) IPF map revealing that the entire pillar has twinned, (e) side view of a micropillar which underwent basal slip even when the highest SF for basal slip was only 0.06 (ϕ = 86°).
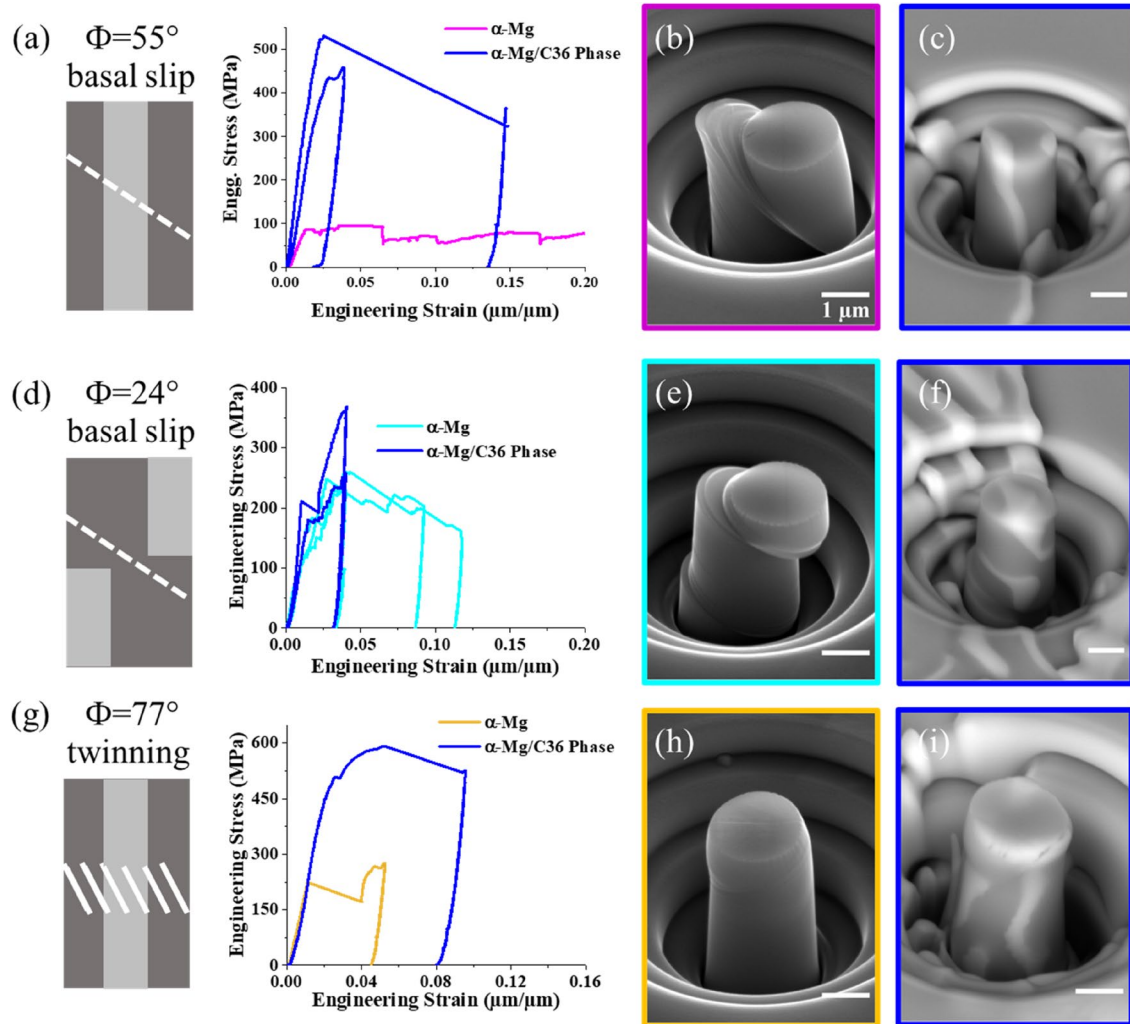
Figure 5: Engineering stress–strain curves of Mg and Mg/C36 Laves phase micropillars with representative micrographs of corresponding micropillars (for more micrographs see Figure SM 2). On the left, the three major cases depicted here are drawn schematically: (a–c) geometric alignment of Mg and C36 phase obstructing through-thickness deformation along the softer Mg phase in basal slip only; (d–f) deformation in case of continuous Mg deformation path by basal slip and (g–i) co-deformation in case of deformation dominated by extension twinning in the Mg matrix. All six scale bars (white lines) represent a length of 1 μm.

restricted the deformation via basal slip in that region of the micropillar.

Similarly, the yield stress of micropillars oriented for extension twinning also increased due to the presence of the Laves phase [Fig. 5(g–i)]. Specifically, $\sigma_{0.2}$ increased from ∼ 220 MPa for a pillar containing only α-Mg [Fig. 5(h)] to ∼ 450 MPa for a pillar containing Laves phase and α-Mg phase [Fig. 5(i)].

Across all pillars tested, the effect of the geometrical alignment of the two phases therefore appears to be more important than the volume fraction of Laves phase in the micropillar with the complete obstruction of an easy deformation path inside the Mg matrix giving maximum strengthening and co-deformation with plasticity in the C36 phase or along an interface in the cases where the Mg phase cannot deform to give a through-thickness shape change of the pillar by itself.

## Co-deformation of the α-Mg and cubic C15 CaAl$_2$ Laves phase

In contrast to the fine Mg/C36 composite in the as-cast material, the annealed state allowed the preparation of micropillars consisting entirely of either Mg or CaAl$_2$ Laves phase as well as a combination of the two. A direct comparison (Fig. 6) between monolithic and two-phase pillars milled in adjacent grains of the two phases and at their interface, respectively, gave a much higher yield stress for the CaAl$_2$ phase ($\sigma_{0.2} \approx 3$ GPa) compared with the α-Mg matrix ($\sigma_{0.2} \sim 130$ MPa) and an intermediate value for a pillar containing Mg/CaAl$_2$ interfaces.

Only a single case of slip transfer visible at the micropillar surface was observed [Fig. 6(g)], although it could not be characterised in more detail due to its position at the very bottom of the micropillar. Again, the pillars showed very little
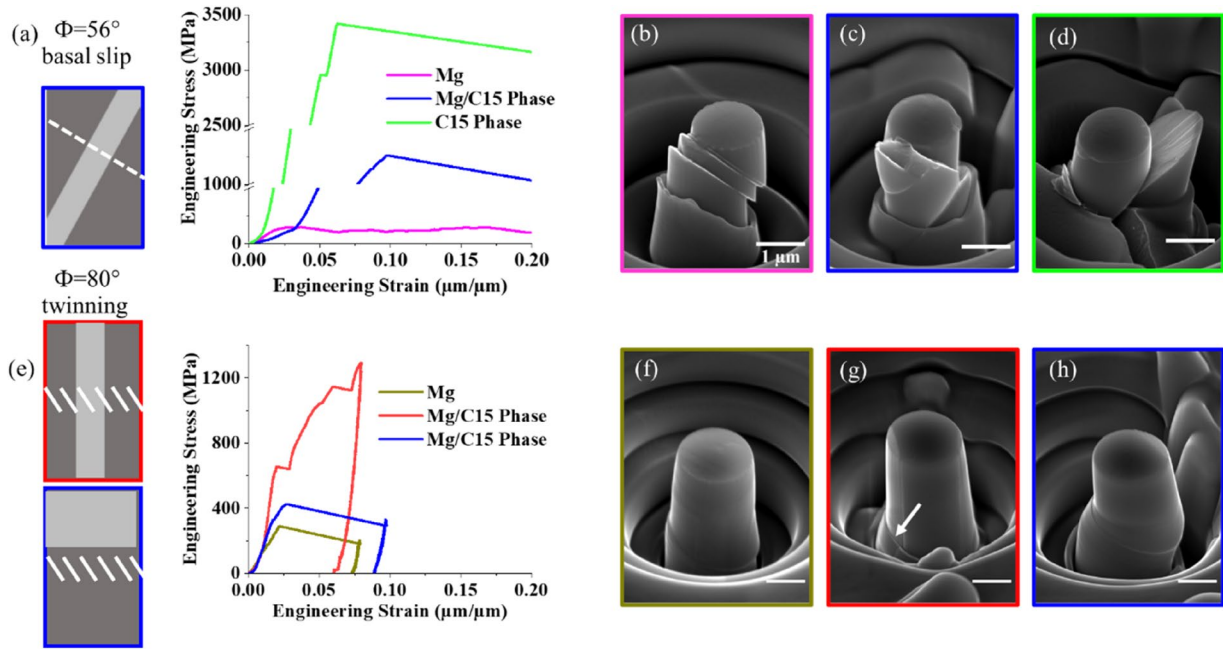
Figure 6: (a) Engineering stress strain curves of micropillars oriented for basal slip containing α-Mg phase, α-Mg/CaAl$_2$ phase mixture, and CaAl$_2$ phase. (b), (c), and (d) are the micrographs of micropillars containing α-Mg phase, α-Mg/CaAl$_2$, and CaAl$_2$ phase, respectively. Both (b) and (c) were milled into the same Mg grain which has high Schmid factor for basal slip. (e) Engineering stress strain curves of micropillars containing the α-Mg phase (φ = 80°) and a Mg/CaAl$_2$ interface (f), (g) and (h) are the SE images of the deformed micropillars. The frame colours of (f), (g) and (h) correspond to the respective stress–strain curves. The white arrow in (g) highlights the point of slip transfer from Mg to CaAl$_2$. Scale bars represent the length of 1 μm.
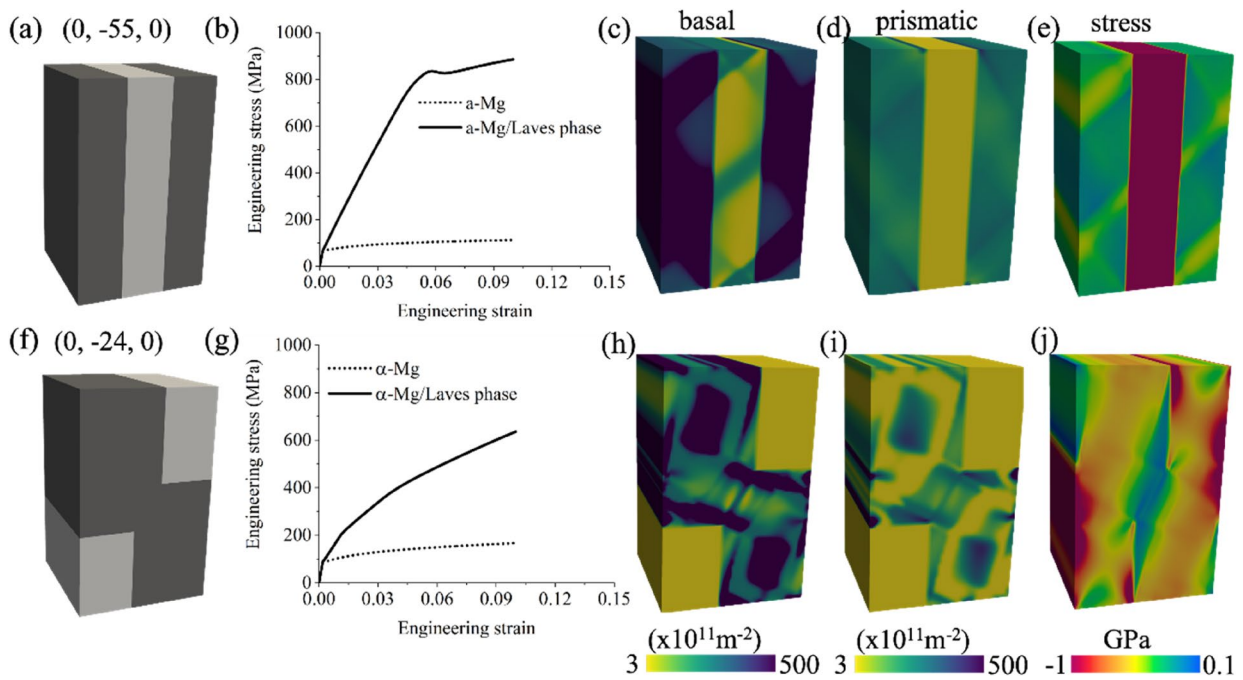
Figure 7: Simulated mechanical responses and spatial distribution of basal, prismatic dislocation densities, and the stress along the compression direction, based on full-field crystal plasticity modelling of the micropillars. (a) Geometrical model of the micropillar with a C36 intermetallic phase running through the matrix. (b) Simulated engineering stress–strain curves. Spatial distribution of basal (c), prismatic (d) dislocation densities, and stress along the compression direction (e), at a compression strain of 9%. (f–j) show the corresponding results that Laves phase is only present in a portion of the micropillar.

strengthening where a continuous deformation path through the Mg matrix existed [Fig. 6(h)] and corresponding stress strain curve) and an intermediate value where the CaAl$_2$ phase could not be circumvented easily.

The experimental results were further compared with the simulated pillars using full-field dislocation density-based crystal plasticly model. For that purpose, two 3D geometrical models were created with different geometric alignment of intermetallic phases, as shown in [Fig. 7(a and f)].

In [Fig. 7(a)], the Laves phase ran through the matrix, while in [Fig. 7(f)] the Laves phase was only present in a portion of the micropillar. In both micropillars, the volume fraction of the Laves phase was 33.3%. It is clear that, for the same volume fraction, a higher flow stress was attained when the Laves phase was present in a top to bottom morphology. Differences with respect to the experimental data mainly result from the discrete nature of flow in experiments, with shear localising on individual planes. This is not captured in the distribution of dislocations and the resulting flow curves in the simulation.

Discussion

Deformation of the α-Mg(Al, Ca) phase

We found that the Mg matrix phase contained about 1.2% Al and a small amount of Ca below the limit of quantitative detection by EDS. This is consistent with expectations based on the solubility of the two elements [14]. In addition, we found precipitates of CaAl$_2$, presumably, parallel to the basal plane which have been described before [8, 11, 12]. In the light of these features, we set out to characterise the orientation dependence of flow in the α-Mg phase in terms of the dominant deformation mechanism (dislocation slip or twinning) and the associated critical resolved shear stresses.

We observed the expected anisotropy [see Fig. 3(a and b)] with the yield stress increasing as the declination angle of the c-axis towards the compression direction tilts from 0° towards 90°. This is because the Schmid factor, m_S, for basal slip is reduced and higher stresses are required to reach the τ_{CRSS} for basal slip. Further, it can be seen in [Fig. 3(a)] that the pillar with a declination angle of ϕ–6° (black curve), exhibited no significant strain bursts in the stress–strain curve, but showed a rather continuous transition from the elastic to the plastic region and a higher strain hardening. The highest Schmid factor for basal slip in this pillar was ~ 0.09, but even then, some basal slip traces were observed on the surface of a deformed micro-pillar. The strong work hardening in such a pillar likely reflects simultaneous activation of non-basal (pyramidal) slip systems, which is usually associated with pillars milled in orientations with ϕ approaching 0° [48]. The τ_{CRSS} for basal slip was measured as 58 ± 19 MPa, in good agreement with the earlier reported values of ~ 51 MPa by Wang et al. [26] for
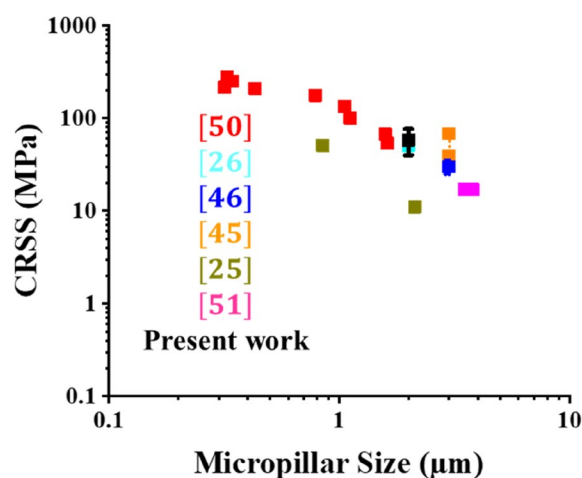
Figure 8: Comparison of CRSS values for basal slip observed in this work and reported in existing literature.

micropillars of similar geometry and size in Mg5%Zn alloy. A more detailed comparison of the CRSS for basal slip with values reported in the literature is presented in Fig. 8. These values are well above those observed in macroscopic tests [16, 17] due to the well-known size effect [45–47, 49–51]. The size effect occurs because of the small number of dislocations sources and the truncation of the moving dislocation arms associated with the small volume and/or with the scarcity of mobile dislocations [27, 45].

The mechanical behaviour of the α-Mg phase in both as-cast and heat-treated states have also been compared. As the amount of Al is similar in both as-cast and heat treated α-Mg, the mechanical response of both phases should be similar. This is indeed what is observed and presented in the Supplementary Materials in Figure SM 3.

The scatter in yield stress values increased significantly for micropillars with $\phi \geq 77°$ (Fig. 3), i.e. away from those orientations where the measured yield stress can confidently be associated with basal slip. The $\sigma_{0.2}$ for these (for which $\phi \geq 77°$) orientations was 240 ± 90 MPa. A relatively large scatter for a similar orientation was also observed by Wang et al. [26] in Mg5%Zn and by Wang et al. [27] in a Mg–0.2Ca–1.8Zn alloy. They [27] related the observed scatter to the initial misalignment between the indenter and the micropillar surface as twin nucleation is very sensitive to localised stresses. Moreover, as presented in [Fig. 4(a–d)], the entire pillar underwent deformation twinning when the declination angle was ($\phi \approx 89°$). However, as shown in [Fig. 4(e)], the pillar appeared to deform via basal slip when ϕ was $\approx 86°$. Additionally, in some pillars, twin-like features were observed on the surface of deformed pillars when ϕ was $\approx 77°$ (Fig. 5). Extension twinning was observed in similar orientations in micropillar compression of pure Mg and its alloys in several recent studies [27, 28, 48,

52–57]. However, the presence of twins in a micropillar can only be confirmed via lift out and additional characterisation by EBSD, TKD or TEM, we therefore did not calculate a CRSS for twinning from the present data, as we only performed TKD on a cross-section of one sample [Fig. 4(d)].

In summary, the observations on the α-Mg micropillars compressed along different orientations conforms entirely with expectations for pillars of the given size and is consistent with reports on microcompression testing in other Mg alloys.

Deformation of the Laves phases

Laves phases (C15, C14 or C36) have a high strength compared to the α-Mg matrix. While to the best of our knowledge no data exists for the $Ca(Mg,Al)_2$ C36 phase in isolation, due to the difficulty of synthesising bulk specimens of sufficient size, we measured here a yield stress of the order of 3 GPa for the $CaAl_2$ C15 phase. This value is within the same range as the values reported by Freund et al. [15] in their work on $CaAl_2$. Using micropillars of a similar diameter of ≈ 2 μm, the yield strength for the $CaMg_2$ Laves phase was found to be ≈ 1.25 GPa, with a corresponding CRSS for basal slip of ≈ 520 GPa [4]. A consistent difference in the micro hardness of $CaAl_2$ and $CaMg_2$ was reported by Rokhlin et al. [5]. The difference between the hardness of the $CaMg_2$ and $CaAl_2$ phases is also evident in a comparison of work by Zehnder et al. [4] and Freund et al. [15]. Zehnder et al. [4] reported a hardness of ≈ 3.4 ± 0.2 GPa for $CaMg_2$, while Freund et al. [15] reported a hardness of 4.9 ± 0.7 GPa for the $CaAl_2$ phase, both at room temperature. In the binary Nb–Co system, all three Laves phases exist as $NbCo_2$ and no significant dependence on the crystal structure was found in indentation across

a diffusion couple containing all three phases [58, 59]. In our case, we change the B element of the general AB_2 Laves phase stoichiometry from predominately Mg (C14) to a mixture of Mg and Al (C36) to predominately Al (C15). We would therefore expect the CRSS values for the C36 Laves phases to be within the range of values reported for the C14 and C15 Laves phases.

In principle, we expect all three Laves phases to act as efficient strengthening phases and this is in fact what we observed in all micropillars containing both phases (α-Mg and Laves phase). Using the image of simple composite deformation, the micropillar strength is determined by the way the two phases are arranged geometrically, with an efficient strengthening only achieved where deformation along the 'weakest link' of a continuous soft phase with a suitable deformation path (basal slip in Mg) is prevented (Figs. 5 and 6).

(Co)-Deformation and reinforcement potential in bulk alloys

Following the characterisation of the Mg(Al, Ca) matrix phase's deformation and the deformation of the Laves phases, we focus on the strengthening potential of the latter within a dual phase microstructure. In this context, the two most important aspects to consider are: (1) Can strengthening be achieved in such a way that the matrix is shielded from excessive stresses? (2) Can the desired phase be easily obtained in a morphology that allows effective stress transfer to the reinforcement phase?

To address the first question, on whether strengthening is achieved in the composite pillars, we approximated the volume fraction of Laves phase in each pillar from the surface area fraction (see Supplementary Materials, Figure SM
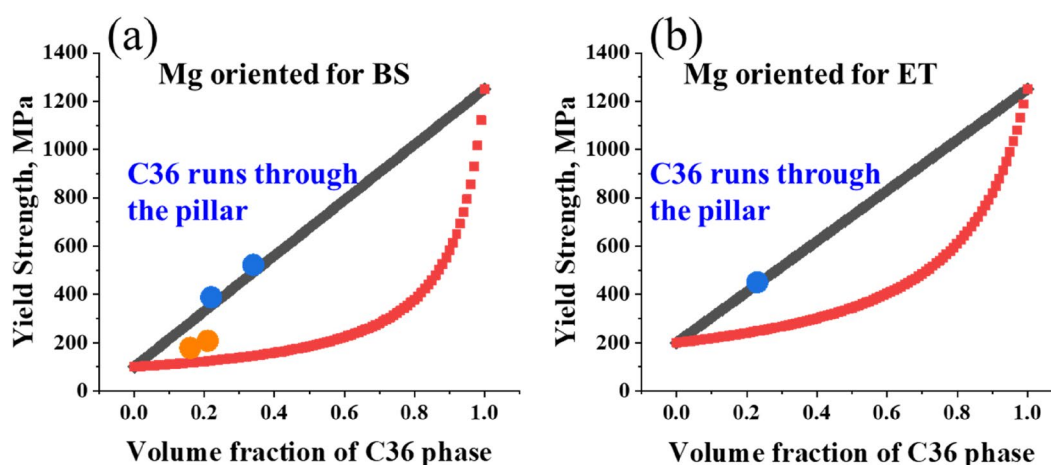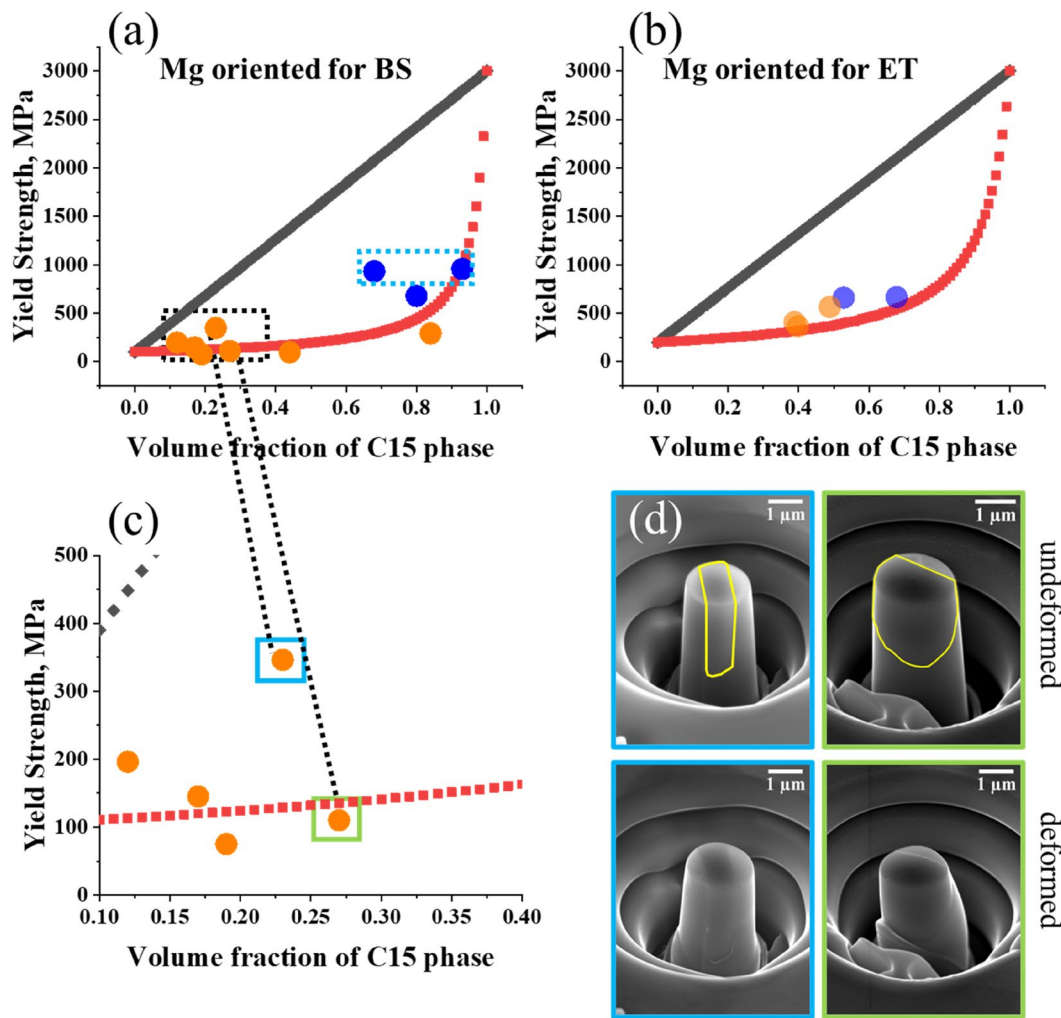

Figure 9: Prediction and measurement of the yield stress in composite pillars with C36 Laves phase where Mg is oriented for basal slip (BS) and extension twinning (ET). Black lines and red curves in (a) and (b) represent the estimated upper and lower bounds for Mg-C36 composite micropillars after applying iso-strain and iso-stress conditions. Blue and orange dots represent the geometry of C36 Laves phase when it runs through the pillar (blue dots) and when it is present only in a portion of the pillar (orange dots). Blue and orange dots in (a) are for the curves presented in Fig. 5(a) and (d) while blue dot in (b) represent the data presented in Fig. 5(g). The micropillars for which the data is presented here and in Fig. 5 are shown from different sides in Figure SM 2.

4) and determined whether at least one continuous segment was observed along its length or not. This effectively divides the pillars into two categories, namely one in which a cross-section of only Mg exists that cannot share the load towards the Laves phase and which has a free path for dislocation slip or twinning, and a second, in which the axial load can be carried along the pillar length in a Laves phase segment that also acts to inhibit slip or twinning (indicated as orange and blue points respectively in Fig. 9). These two scenarios, as ideal cases, correspond to the iso-stress and iso-strain assumptions, respectively. For the pillars investigated here, we found that in iso-stress condition, the predicted lower bound on the strength is well reproduced in the pillars. To estimate stresses for these conditions, the strength of pure Mg phase oriented for basal slip was taken as 100 MPa and as 200 MPa in case

Mg is oriented for twinning. The yield strength for the C36 phase was assumed as that of the C14 phase (≈1250 MPa, see [4]). The resulting upper and lower bounds of the strength representing the iso-strain and iso-stress conditions for composite micropillars are given by grey and red symbols in Fig. 9.

For the pillars which may approach an iso-strain condition, the available microstructures from which the pillars were cut affect the results: for the C36 reinforced pillars, continuous segments were found at low volume fractions and good agreement with the predicted upper bound of the strength was seen. These results also correspond well to crystal plasticity simulations performed to assess the expected pillar behaviour more quantitatively by taking the strong anisotropy of slip in the Mg phase into account (see Fig. 7). The simple predictions from

Figure 10: Prediction and measurement of the yield stress in composite pillars with C15 Laves phase where Mg is oriented for basal slip (BS) and extension twinning (ET). Grey and red symbols in (a) and (b) represent the estimated upper and lower bounds for Mg-C15 composite micropillars after applying iso-strain and iso-stress conditions. A magnified view of the portion indicated by the dotted black rectangle in (a) is presented in (c). Light blue and green boxes indicate the two data points corresponding to the composite pillars presented in (d). The undeformed and deformed micropillars whose $\sigma_{0.2}$ is denoted by the blue dots and enclosed by dotted light blue rectangle in (a) are presented in Figure SM 5.

composite models therefore seem sufficient for the purpose of this investigation overall.

For the C15 phase and the two present precipitate shapes, only the irregularly shaped particles were large enough to span the entire length of a pillar and occurred only at large volume fractions of 50% and above. In these cases, we found that the upper bound was not reached, but instead a maximum stress of the order of 1 GPa was achieved (Fig. 10). This stress is above that achieved in the Mg/C36 pillars and of the order the upper bound expected to be achievable with C36 reinforcement, but a third of the bulk C15 strength.

Both phases therefore provide load shielding and additional strength in combination with the Mg matrix, but in the volume of tens of µm [3] investigated here, optimal strength is not achieved in either composite. While in case of the C36 phase, the phase morphology prevents higher volume fractions, in case of the C15 phase it precludes the realisation of well-defined iso-stress conditions, rather, the micropillars fail at lower stresses, possibly due to stress concentrations along the jagged interfaces of the brittle phase.

In a bulk microstructure, conditions of similarly efficient load sharing as in micropillars with a continuous Laves phase running from top to bottom are only achieved by a continuous intermetallic skeleton, otherwise hardening must rely on the obstruction of dislocation motion. The skeleton-like (continuous) morphology of Laves phase directly after casting is promoted with increasing Ca/Al ratio [8] but the $CaAl_2$ phase is found primarily at low Ca/Al ratios [30]. The C36 and C14 phases appear at high Ca/Al ratio and form a skeleton in the Mg matrix in which strut thickness and connectivity can then be tuned by solidification rate and alloy content, respectively. In these alloys, the C15 phase can be obtained also, but upon extended heat treatment and slow cooling, as performed here, and occurs in the form of discontinuous particles. The mechanical behaviour of such microstructures is consistent with particle composites, both in terms of dislocation hardening models and the prevalent iso-stress condition making these comparatively soft, However, it has been reported in recent literature that the presence of C15 phase within Mg matrix also leads to considerable work-hardening in Mg–Al–Ca alloys [14, 60]. The C15 phase reinforced Mg–Al–Ca alloys can therefore demonstrate a very good combination of room temperature strength and ductility [14, 60].

Owing to the difficulty of obtaining pillars with controlled volume fractions and morphologies of both phases for the most highly loaded iso-strain conditions, we were not able to assess the mechanisms of plastic co-deformation in more detail. In particular, we had initially hoped to connect this work to atomistic modelling activities that revealed possible co-deformation and its thermally activated nature [10], consistent with nanoindentation across two phase regions of the microstructure and a decrease in the occurrence of brittle cracks formed under normal stress in quasi-static tensile deformation of bulk specimens at elevated temperature and low rate [6, 61]. For the Mg/C36 pillars with a continuous Laves phase resulting in a yield stress of the order of the expected iso-strain condition, this may be possible in the future, but likely restricted to elevated temperature testing and ideally in a displacement-controlled device.

Conclusions

We investigated the deformation and co-deformation of a α-Mg(Al,Ca) solid solution matrix with small precipitates deformed along different crystal orientations and its co-deformation with the cubic $CaAl_2$ C15 and hexagonal $Ca(Mg,Al)_2$ C36 Laves phases. Our findings and conclusions include:

1. The CRSS for basal slip in ≈ 2 µm α-Mg(Al,Ca) micropillars at 58 ± 19 MPa corresponds closely to that of related alloys and twinning is introduced where the compression direction approaches a direction that is perpendicular to the c-axis.
2. Both, the C36 and C15 Laves phases delay the onset of basal slip in the α-Mg phase and also provide significant strengthening where the Mg phase is oriented for extension twinning.
3. The C15 phase is intrinsically harder to deform plastically but both the C15 and C36 phase are much harder than the Mg matrix and therefore provide appreciable strengthening to composite micropillars.
4. The amount of strengthening is consistent with expectations for composite models. It depends in particular on volume fraction and whether the intermetallic spans the length of the micropillar (hard case / near iso-strain conditions) or not (soft case / near iso-stress condition).

Experimental methods

Sample preparation and microscopy

The raw materials were molten in a steel crucible inside a vacuum induction furnace under a protective atmosphere of Ar. The melt was solidified and cooled in a Cu mould inside the furnace under protective atmosphere. The chemical composition of the as-cast alloy was measured using wet chemical analysis to be Mg–4.65Al–2.82Ca alloy. To increase the size of the intermetallic struts, a heat treatment of the as-cast alloy was carried out at 500 °C for 48 h in Ar atmosphere followed by cooling in air. This resulted not only in the coarsening of the intermetallic structure but also in the transformation from the C36 to the C15 phase. We refer to these two states as the as-cast and annealed conditions.

TABLE 1: Material parameters for the constitutive model.

Crystal plasticity model	b (m)	v_0 (ms^{-1})	Q_a (J)	τ_P (Pa)	p	q
Basal	3.20×10^{-10}	1.0×10^{-5}	7.0×10^{-20}	2.0×10^{7}	1.0	1.0
Prismatic	3.20×10^{-10}	1.0×10^{-5}	7.0×10^{-20}	6.8×10^{7}	1.0	1.0
Pyramidal	6.11×10^{-10}	1.0×10^{-5}	7.0×10^{-20}	1.4×10^{8}	1.0	1.0

Two specimens for microstructure analysis and micropillar milling were cut using electric discharge erosion from the as-cast block, one of which was subjected to the heat treatment. The samples were ground using 2000 and 4000 SiC emery papers, followed by mechanical polishing using 3 and 1 μm diamond suspension. To remove the deformation layer, the samples were subjected to electro-polishing using Struers AC-II electrolyte. The samples were etched for 60 s at ~ − 20 °C and 15 V. The electro-polished surface was then subjected to mechanical polishing using Struers OPU (colloidal suspension of SiO$_2$ nano particles) for ~ 60 s to remove the waviness arising from electro-polishing of the dual phase material.

SE imaging in scanning electron microscopes (SEM, FEI Helios 600i and Zeiss LEO1530) was used to analyse the microstructures. EBSD was used to measure the crystallographic orientations of the α-Mg matrix. Due to the small size of the intermetallic Laves phase in the as-cast alloy, it was not possible to measure the orientation of the Laves phase. An accelerating voltage of 5–10 kV was used for SE imaging while EBSD was done at 20 kV.

TKD was done on the cross-sections of a selected micropillar (see Fig. 4). For this purpose, the pillars' cross-sections were lifted out of the original sample and were placed on a TEM grid. They were thinned down to a thickness of ~ 300 nm using FIB with currents ranging from 230 to 80 pA. A current of 80pA, was used for the final polishing steps. TKD was performed on the cross-sections with a step size of 50–60 nm at 30 kV and 5.5 nA. All EBSD data was analysed using OIM Analysis 7.3.1 (EDAX).

Microcompression

Micropillars of ~ 1.6–2 μm diameter and ~ 3.5–4.5 μm height were milled in matrix grains with different orientations, where the inclination of the c-axis to the compression direction was varied from 0 to 90°, using FIB milling. Stress and strain calculations were performed using the actual dimensions of the pillars determined from SEM images. The top diameter of the pillars was used for stress calculation. The cylindrical pillars were milled using concentric circles with a decreasing ion beam current from 9.3 nA to 80 pA at an accelerating voltage of 30 kV. The pillar taper angle was less than 2° for most pillars.

The micropillars were compressed in two different load-controlled nanoindenters (iNano and InSEM III; Nanomechanics Inc., USA) at a loading rate of 0.05 mN/s and using a flat punch diamond indenter with a diameter of 10 μm. The Sneddon correction was applied to the depth data to minimise the effect of elastic deformation of substrate and indenter as discussed in [62]. The tests were stopped after a significant strain burst was observed in the load-depth curve. The slip systems were analysed using the code and method already presented in [44], after adjustment for the hexagonal Mg phase. The micropillars before and after deformation were imaged from at least three different directions at a tilt angle of 45°.

Crystal plasticity modelling

A full-field dislocation density-based crystal plasticity model was employed to reveal more insights into the co-plastic deformation mechanisms and micromechanics of the micropillar with different geometric alignment of intermetallic phases. The model is briefly outlined in the following. For details readers are referred to references [63–66].

The total deformation gradient **F** is decomposed into an elastic part **F**$_e$ and a plastic part **F**$_p$, as **F** = **F**$_e$**F**$_p$. The evolution of **F**$_p$ is related to the plastic velocity gradient **L**$_p$ according to the flowing rule $\dot{\mathbf{F}}_p = \mathbf{L}_p \mathbf{F}_p$. **L**$_p$ is given by the superposition of shear on all slip systems, as.

$$L_p = \sum_{\alpha=1}^{N_S} \dot{\gamma}_S^\alpha \, \mathrm{m}_S^\alpha \otimes \mathrm{n}_S^\alpha$$

where $\dot{\gamma}_s^\alpha$ describes the shear rate on slip system α, and $\mathbf{m}_s^\alpha$ and $\mathbf{n}_s^\alpha$ indicate the slip direction and the slip plane normal of the N_s slip systems. The shear rate of mobile dislocations on a slip system can be calculated based on the Orowan equation as:

$$\dot{\gamma} = \rho_m b v_0 \exp\left[-\frac{Q_a}{k_B T}\left\{1 - \left(\frac{|\tau_{eff}|}{\tau_P}\right)^p\right\}^q\right] \mathrm{sign}(\tau),$$

where ρ_m is the mobile dislocation density, b is the magnitude of the Burgers vector, and v_0 is the reference dislocation glide velocity, Q_a is the activation energy for dislocation glide to overcome the obstacles, k_B is the Boltzmann constant, T is temperature, τ_P is the Peierls stress, and p and q are fitting parameters. τ_{eff} is the effective resolved shear stress as the driving force for dislocation slip, and is calculated as the resolved stress reduced by the passing stress.

Two 3D geometrical models with different geometric alignment of intermetallic phases were created (Fig. 7). The Euler

angle of the matrix was (0, − 55, 0) and (0, − 24, 0), respectively, for the micropillar in Fig. 7(a) and (f). In the current work, basal $<a>$ ({0001} $<11\bar{2}0>$), prismatic $<a>$ ({$10\bar{1}0$} $<11\bar{2}0>$), and pyramidal $<c+a>$ ({$\bar{1}122$} $<\bar{1}123>$) slip systems are considered to accommodate the plastic deformation. Monotonic compression loading was applied to the model, at a strain rate of $0.001\ \text{s}^{-1}$. The material parameters used are listed in Table 1. It is worth noting that the plastic deformation of the Laves phase was also considered in the current work, where the threshold stress for activating the dislocation (τ_P) in Laves phase was set to be 1GPa. The other material parameters are the same as those with Mg matrix.

Acknowledgments

Funding

Data availability

Data can be provided on request.

Declarations

Conflict of interest On behalf of all authors, the corresponding author states that there is no conflict of interest.

Open Access

Supplementary Information

The online version contains supplementary material available at https://doi.org/10.1557/s43578-023-01082-x.

References

1. B. Kondori, R. Mahmudi, Effect of Ca additions on the microstructure and creep properties of a cast Mg–Al–Mn magnesium alloy. Mater. Sci. Eng.: A **700**, 438 (2017)

2. D. Amberger, P. Eisenlohr, M. Göken, Microstructural evolution during creep of Ca-containing AZ91. Mater. Sci. Eng.: A **510–511**, 398 (2009)

3. Y. Terada, R. Sota, N. Ishimatsu, T. Sato, K. Ohori, A Thousandfold creep strengthening by Ca addition in die-cast AM50 magnesium alloy. Metall. Mater. Trans. A **35A**, 4 (2004)

4. C. Zehnder, K. Czerwinski, K.D. Molodov, S. Sandlöbes-Haut, J.S.K.L. Gibson, S. Korte-Kerzel, Plastic deformation of single crystalline C14 Mg_2Ca Laves phase at room temperature. Mater. Sci. Eng.: A **759**, 754 (2019)

5. L.L. Rokhlin, T.V. Dobatkina, N.I. Nikitina, I.E. Tarytina, Calcium-alloyed magnesium alloys. Met. Sci. Heat Treat. **51**(3), 164 (2009)

6. M. Zubair, S. Sandlöbes-Haut, M. Lipińska-Chwałek, M.A. Wollenweber, C. Zehnder, J. Mayer, J.S.K.L. Gibson, S. Korte-Kerzel, Co-deformation between the metallic matrix and intermetallic phases in a creep-resistant Mg-3.68Al-3.8Ca alloy. Mater. Des. **210**, 110113 (2021)

7. M. Freund, D. Andre, C. Zehnder, H. Rempel, D. Gerber, M. Zubair, S. Sandlöbes-Haut, J.S.K.L. Gibson, S. Korte-Kerzel, Plastic deformation of the $CaMg_2$ C14-Laves phase from 50–250°C. Materialia **20**, 101237 (2021)

8. M. Zubair, S. Sandlöbes, M.A. Wollenweber, C.F. Kusche, W. Hildebrandt, C. Broeckmann, S. Korte-Kerzel, On the role of Laves phases on the mechanical properties of Mg-Al-Ca alloys. Mater. Sci. Eng.: A **756**, 272 (2019)

9. M. Zubair, S. Sandlöbes-Haut, M.A. Wollenweber, K. Bugelnig, C.F. Kusche, G. Requena, S. Korte-Kerzel, Strain heterogeneity and micro-damage nucleation under tensile stresses in an Mg–5Al–3Ca alloy with an intermetallic skeleton. Mater. Sci. Eng.: A. **767**, 138414 (2019)

10. J. Guénolé, M. Zubair, S. Roy, Z. Xie, M. Lipińska-Chwałek, S. Sandlöbes-Haut, S. Korte-Kerzel, Exploring the transfer of plasticity across Laves phase interfaces in a dual phase magnesium alloy. Mater. Des. **202**, 109572 (2021)

11. N.D. Saddock, A. Suzuki, J.W. Jones, T.M. Pollock, Grain-scale creep processes in Mg–Al–Ca base alloys: implications for alloy design. Scr. Mater. **63**(7), 692 (2010)

12. A. Suzuki, N.D. Saddock, J.R. TerBush, B.R. Powell, J.W. Jones, T.M. Pollock, Precipitation Strengthening of a Mg-Al-Ca–based AXJ530 die-cast alloy. Metall. Mater. Trans. A **39**(3), 696 (2008)

13. D. Amberger, P. Eisenlohr, M. Goken, On the importance of a connected hard-phase skeleton for the creep resistance of Mg alloys. Acta Mater. **60**(5), 2277 (2012)

14. M. Zubair, M. Felten, B. Hallstedt, M. Vega Paredes, L. Abdel-laoui, R. Bueno Villoro, M. Lipinska-Chwalek, N. Ayeb, H. Springer, J. Mayer, B. Berkels, D. Zander, S. Korte-Kerzel, C. Scheu, S. Zhang, Laves phases in Mg-Al-Ca alloys and their effect on mechanical properties. Mater. Des. **225**, 111470 (2023)

15. M. Freund, D. Andre, P.L. Sun, C.F. Kusche, S. Sandlöbes-Haut, H. Springer, S. Korte-Kerzel, Plasticity of the C15-CaAl$_2$ Laves phase at room temperature. Mater. Des. **225**, 111504 (2023)

16. H. Conrad, W.D. Robertson, Effect of temperature on the flow stress and strain-hardening coefficient of magnesium single crystals. JOM **9**(4), 503 (1957)

17. A. Akhtar, E. Teghtsoonian, Solid solution strengthening of magnesium single crystals—I alloying behaviour in basal slip. Acta Metall. **17**(11), 1339 (1969)

18. Q. Yu, J. Zhang, Y. Jiang, Direct observation of twinning–detwinning–retwinning on magnesium single crystal subjected to strain-controlled cyclic tension–compression in [0 0 0 1] direction. Philos. Mag. Lett. **91**(12), 757 (2011)

19. A. Chapuis, J.H. Driver, Temperature dependency of slip and twinning in plane strain compressed magnesium single crystals. Acta Mater. **59**(5), 1986 (2011)

20. R.E. Reed-Hill, W.D. Robertson, Deformation of magnesium single crystals by nonbasal slip. JOM **9**(4), 496 (1957)

21. A. Akhtar, E. Teghtsoonian, Solid solution strengthening of magnesium single crystals—ii the effect of solute on the ease of prismatic slip. Acta Metall. **17**(11), 1351 (1969)

22. T. Obara, H. Yoshinga, S. Morozumi, {ll-22}<-1-123> Slip system in magnesium. Acta Metall. **21**(7), 845 (1973)

23. C.M. Byer, B. Li, B. Cao, K.T. Ramesh, Microcompression of single-crystal magnesium. Scr. Mater. **62**(8), 536 (2010)

24. F. Hiura, Work Hardening and Latent Hardening of Mg Single Crystals under Uniaxial Deformation at 298K, in Materials Science and Engineering, (McMaster University, City, 2015)

25. Z.H. Aitken, H. Fan, J.A. El-Awady, J.R. Greer, The effect of size, orientation and alloying on the deformation of AZ31 nanopillars. J. Mech. Phys. Solids **76**, 208 (2015)

26. J. Wang, N. Stanford, Investigation of precipitate hardening of slip and twinning in Mg5%Zn by micropillar compression. Acta Mater. **100**, 53 (2015)

27. J. Wang, Y. Chen, Z. Chen, J. Llorca, X. Zeng, Deformation mechanisms of Mg-Ca-Zn alloys studied by means of micropillar compression tests. Acta Mater. **217**, 117151 (2021)

28. N. Li, L. Yang, C. Wang, M.A. Monclús, D. Shi, J.M. Molina-Aldareguía, Deformation mechanisms of basal slip, twinning and non-basal slips in Mg–Y alloy by micropillar compression. Mater. Sci. Eng.: A **819**, 141408 (2021)

29. S. Sanyal, M. Paliwal, T.K. Bandyopadhyay, S. Mandal, Evolution of microstructure, phases and mechanical properties in lean as-cast Mg–Al–Ca–Mn alloys under the influence of a wide range of Ca/Al ratio. Mater. Sci. Eng.: A **800**, 140322 (2021)

30. S.M. Liang, R.S. Chen, J.J. Blandin, M. Suery, E.H. Han, Thermal analysis and solidification pathways of Mg–Al–Ca system alloys. Mater. Sci. Eng.: A **480**(1), 365 (2008)

31. Z.T. Li, X.D. Zhang, M.Y. Zheng, X.G. Qiao, K. Wu, C. Xu, S. Kamado, Effect of Ca/Al ratio on microstructure and mechanical properties of Mg-Al-Ca-Mn alloys. Mater. Sci. Eng.: A **682**, 423 (2017)

32. L. Zhang, K. Deng, K. Nie, F. Xu, K. Su, W. Liang, Microstructures and mechanical properties of Mg–Al–Ca alloysaffected by Ca/Al ratio. Mater. Sci. Eng.: A. **636**, 279 (2015)

33. B. Kondori, R. Mahmudi, Effect of Ca additions on the microstructure, thermal stability and mechanical properties of a cast AM60 magnesium alloy. Mater. Sci. Eng.: A **527**(7), 2014 (2010)

34. A. Suzuki, N.D. Saddock, J.W. Jones, T.M. Pollock, Structure and transition of eutectic (Mg, Al)2Ca Laves phase in a die-cast Mg–Al–Ca base alloy. Scr. Mater. **51**(10), 1005 (2004)

35. A. Suzuki, N.D. Saddock, J.W. Jones, T.M. Pollock, Solidification paths and eutectic intermetallic phases in Mg–Al–Ca ternary alloys. Acta Mater. **53**(9), 2823 (2005)

36. S. Sanyal, M. Paliwal, T.K. Bandyopadhyay, S. Mandal, Evolution of microstructure, phases and mechanical properties in lean as-cast Mg–Al–Ca–Mn alloys under the influence of a wide range of Ca/Al ratio. Mater. Sci. Eng.: A. **800**, 140322 (2021)

37. A.A. Luo, M.P. Balogh, B.R. Powell, Creep and microstructure of magnesium-aluminum-calcium based alloys. Metall. Mater. Trans. A **33**(3), 567 (2002)

38. H.A. Elamami, A. Incesu, K. Korgiopoulos, M. Pekguleryuz, A. Gungor, Phase selection and mechanical properties of permanent-mold cast Mg–Al–Ca–Mn alloys and the role of Ca/Al ratio. J. Alloys Compd. **764**, 216 (2018)

39. M. Zubair: Co-deformation of metallic and intermetallic phases in Mg–Al–Ca alloys. RWTH, City, (2022)

40. N. Takata, H. Ghassemi Armaki, Y. Terada, M. Takeyama, K.S. Kumar, Plastic deformation of the C14 Laves phase (Fe, Ni)$_2$Nb. Scripta Mater. **68**(8), 615 (2013)

41. A. Tehranchi, M. Lipinska-Chwalek, J. Mayer, J. Neugebauer, T. Hickel: Phase stability and defect studies of Mg-based Laves phases using defect phase diagrams. City, (2023)

42. S. Amerioun, S.I. Simak, U. Häussermann, Laves-Phase structural changes in the system CaAl$_{2-x}$Mg$_x$. Inorg. Chem. **42**(5), 1467 (2003)

43. M. Heller, J.S.K.L. Gibson, R. Pei, S. Korte-Kerzel, Deformation of μm- and mm-sized Fe2.4wt%Si single- and bi-crystals with a high angle grain boundary at room temperature. Acta Mater. **194**, 452 (2020)

44. J.S.K.L. Gibson, R. Pei, M. Heller, S. Medghalchi, W. Luo, S. Korte-Kerzel, Finding and characterising active slip systems: a short review and tutorial with automation tools. Materials (2021). https://doi.org/10.3390/ma14020407

45. C.M. Byer, K.T. Ramesh, Effects of the initial dislocation density on size effects in single-crystal magnesium. Acta Mater. **61**(10), 3808 (2013)

46. K.E. Prasad, K. Rajesh, U. Ramamurty, Micropillar and macropillar compression responses of magnesium single crystals oriented for single slip or extension twinning. Acta Mater. **65**, 316 (2014)

47. Y. Liu, N. Li, M. Arul Kumar, S. Pathak, J. Wang, R.J. McCabe, N.A. Mara, C.N. Tomé, Experimentally quantifying critical stresses associated with basal slip and twinning in magnesium using micropillars. Acta Mater. **135**, 411 (2017)

48. J. Wu, S. Si, K. Takagi, T. Li, Y. Mine, K. Takashima, Y.L. Chiu, Study of basal < a > and pyramidal < c + a > slips in Mg-Y alloys using micro-pillar compression. Philos. Mag. **100**(11), 1454 (2020)

49. J.Y. Wang, N. Li, R. Alizadeh, M.A. Monclus, Y.W. Cui, J.M. Molina-Aldareguia, J. LLorca, Effect of solute content and temperature on the deformation mechanisms and critical resolved shear stress in Mg-Al and Mg-Zn alloys. Acta Mater. **170**, 155 (2019)

50. J. Ye, R.K. Mishra, A.K. Sachdev, A.M. Minor, In situ TEM compression testing of Mg and Mg–0.2wt.% Ce single crystals. Scripta Mater. **64**(3), 292 (2011)

51. R. Chen, S. Sandlöbes, C. Zehnder, X. Zeng, S. Korte-Kerzel, D. Raabe, Deformation mechanisms, activated slip systems and critical resolved shear stresses in an Mg-LPSO alloy studied by micro-pillar compression. Mater. Des. **154**, 203 (2018)

52. I. Basu, M. Chen, J. Wheeler, R.E. Schäublin, J.F. Löffler, Stacking-fault mediated plasticity and strengthening in lean, rare-earth free magnesium alloys. Acta Mater. **211**, 116877 (2021)

53. J.Y. Wang, J.M. Molina-Aldareguia, J. LLorca, Effect of Al content on the critical resolved shear stress for twin nucleation and growth in Mg alloys. Acta Mater. **188**, 215 (2020)

54. X. Ma, Q. Jiao, L.J. Kecskes, J.A. El-Awady, T.P. Weihs, Effect of basal precipitates on extension twinning and pyramidal slip: a micro-mechanical and electron microscopy study of a Mg–Al binary alloy. Acta Mater. **189**, 35 (2020)

55. G.-D. Sim, K.Y. Xie, K.J. Hemker, J.A. El-Awady, Effect of temperature on the transition in deformation modes in Mg single crystals. Acta Mater. **178**, 241 (2019)

56. J. Jeong, M. Alfreider, R. Konetschnik, D. Kiener, S.H. Oh, In-situ TEM observation of 101ˉ2 twin-dominated deformation of Mg pillars: twinning mechanism, size effects and rate dependency. Acta Mater. **158**, 407 (2018)

57. K. Máthis, M. Knapek, F. Šiška, P. Harcuba, D. Ugi, P.D. Ispánovity, I. Groma, K.S. Shin, On the dynamics of twinning in magnesium micropillars. Mater. Des. **203**, 109563 (2021)

58. W. Luo, C. Kirchlechner, J. Li, G. Dehm, F. Stein, Composition dependence of hardness and elastic modulus of the cubic and hexagonal NbCo$_2$ Laves phase polytypes studied by nanoindentation. J. Mater. Res. **35**(2), 185 (2020)

59. W. Luo, C. Kirchlechner, J. Zavašnik, W. Lu, G. Dehm, F. Stein, Crystal structure and composition dependence of mechanical properties of single-crystalline NbCo$_2$ Laves phase. Acta Mater. **184**, 151 (2020)

60. G. Zhu, L. Wang, J. Wang, J. Wang, J.-S. Park, X. Zeng, Highly deformable Mg–Al–Ca alloy with Al$_2$Ca precipitates. Acta Mater. **200**, 236 (2020)

61. S. Medghalchi, M. Zubair, E. Karimi, S. Sandlöbes-Haut, U. Kerzel, S. Korte-Kerzel, Rate dependence of damage formation in metallic-intermetallic Mg-Al-Ca composites. (2023). https://doi.org/10.48550/arXiv.2303.10477

62. H. Fei, A. Abraham, N. Chawla, H. Jiang, Evaluation of micropillar compression tests for accurate determination of elastic-plastic constitutive relations. J. Appl. Mech. (2012). https://doi.org/10.1115/14006767

63. C. Liu, P. Shanthraj, M. Diehl, F. Roters, S. Dong, J. Dong, W. Ding, D. Raabe, An integrated crystal plasticity–phase field model for spatially resolved twin nucleation, propagation, and growth in hexagonal materials. Int. J. Plast. **106**, 203 (2018)

64. C. Liu, P. Shanthraj, J.D. Robson, M. Diehl, S. Dong, J. Dong, W. Ding, D. Raabe, On the interaction of precipitates and tensile twins in magnesium alloys. Acta Mater. **178**, 146 (2019)

65. C. Liu, F. Roters, D. Raabe, Finite strain crystal plasticity-phase field modeling of twin, dislocation, and grain boundary interaction in hexagonal materials. Acta Mater. **242**, 118444 (2023)

66. F. Roters, M. Diehl, P. Shanthraj, P. Eisenlohr, C. Reuber, S.L. Wong, T. Maiti, A. Ebrahimi, T. Hochrainer, H.O. Fabritius, S. Nikolov, M. Friák, N. Fujita, N. Grilli, K.G.F. Janssens, N. Jia, P.J.J. Kok, D. Ma, F. Meier, E. Werner, M. Stricker, D. Weygand, D. Raabe, DAMASK—The Düsseldorf Advanced Material Simulation Kit for modeling multi-physics crystal plasticity, thermal, and damage phenomena from the single crystal up to the component scale. Comput. Mater. Sci. **158**, 420 (2019)